

# PCCP

Accepted Manuscript



This is an *Accepted Manuscript*, which has been through the Royal Society of Chemistry peer review process and has been accepted for publication.

*Accepted Manuscripts* are published online shortly after acceptance, before technical editing, formatting and proof reading. Using this free service, authors can make their results available to the community, in citable form, before we publish the edited article. We will replace this *Accepted Manuscript* with the edited and formatted *Advance Article* as soon as it is available.

You can find more information about *Accepted Manuscripts* in the [Information for Authors](#).

Please note that technical editing may introduce minor changes to the text and/or graphics, which may alter content. The journal's standard [Terms & Conditions](#) and the [Ethical guidelines](#) still apply. In no event shall the Royal Society of Chemistry be held responsible for any errors or omissions in this *Accepted Manuscript* or any consequences arising from the use of any information it contains.

Cite this: DOI: 10.1039/c0xx00000x

www.rsc.org/xxxxxx

ARTICLE TYPE

## Enhanced up-conversion and temperature-sensing behaviour of Er<sup>3+</sup> and Yb<sup>3+</sup> co-doped Y<sub>2</sub>Ti<sub>2</sub>O<sub>7</sub> by incorporation of Li<sup>+</sup> ions

B. P. Singh,<sup>a</sup> A. K. Parchur,<sup>\*b,c</sup> R. S. Ningthoujam,<sup>d</sup> P. V. Ramakrishna,<sup>e</sup> P. Singh,<sup>a</sup> S. B. Rai<sup>b</sup> and R. Maalej<sup>f</sup>

Received (in XXX, XXX) XthXXXXXXXXXX 20XX, Accepted Xth XXXXXXXXXXXXX 20XX

DOI: 10.1039/b000000x

Y<sub>2</sub>Ti<sub>2</sub>O<sub>7</sub>:Er<sup>3+</sup>/Yb<sup>3+</sup> (EYYTO) phosphors co-doped with Li<sup>+</sup> ions were synthesized by a conventional solid-state ceramic method. The X-ray diffraction studies show that all the Li<sup>+</sup> co-doped EYYTO samples are highly crystalline in nature with pyrochlore face centred cubic structure. The X-ray photon spectroscopy studies reveal that the incorporation of Li<sup>+</sup> ions creates the defects and/or vacancies associated with the sample surface. The effect of Li<sup>+</sup> ions on the photoluminescence up-conversion intensity of EYYTO was studied in detail. The up-conversion study under ~976 nm excitation for different concentrations of Li<sup>+</sup> ions showed that the green and red band intensities were significantly enhanced. The 2 at% Li<sup>+</sup> ion co-doped EYYTO samples showed nearly 15- and 8-fold enhancements in green and red band up-converted intensities than Li<sup>+</sup> ion free EYYTO. The process involved in the up-conversion emission was evaluated in detail by pump power dependence, energy level diagram, and decay analysis. The incorporation of Li<sup>+</sup> ions modified the crystal field around the Er<sup>3+</sup> ions, thus improving the up-conversion intensity. To investigate the sensing application of the synthesized phosphor materials, temperature-sensing performance was evaluated using the fluorescence intensity ratio technique. Appreciable temperature sensitivity was obtained using the synthesized phosphor material, indicating its applicability as a high-temperature-sensing probe. The maximum sensitivity was found to be 0.0067 K<sup>-1</sup> at 363 K.

### 1. Introduction

Lanthanide (Ln<sup>3+</sup>)-doped nano-phosphors have attracted much attention because of their wide applicability in optical filters, laser materials, LEDs, and spectral converters as the next-generation energy-harvesting materials in solar cells and up-conversion luminescent nano-materials.<sup>1-4</sup> The interests in nano-phosphors are increasing because of their superior features such as long-lived luminescence, anti-Stokes shifts, narrow emission bands, high resistance to photo-bleaching, remarkable light penetration depth in tissue, and low toxicity compared to conventional molecular probes such as organic dyes and quantum dots.<sup>5</sup> Ln<sup>3+</sup>-doped nano-phosphors involve intra 4f-4f electronic transitions, providing fascinating features because of abundant energy levels, long lifetimes (~ms to μs) because of the parity-forbidden nature of 4f-4f transitions and a sharp spectral width of ~10 nm. However, the low absorption cross-section of Ln<sup>3+</sup> ions decreases the efficiency of luminescence intensity by direct excitation into the 4f bands. To overcome this problem, Yb<sup>3+</sup> has been used as a prominent sensitizer because of its large absorption cross-section at NIR excitation than Er<sup>3+</sup> and/or Tm<sup>3+</sup> counterpart. Energy is transferred from Yb<sup>3+</sup> to Er<sup>3+</sup>/Tm<sup>3+</sup>. The up-conversion process (two/three-photon process) is observed when subsequent energy transfer (ET) promotes the electrons of Er<sup>3+</sup> and/or Tm<sup>3+</sup> ions to higher energy levels, and radiative decay pathways lead to higher energy, emitting up-converted photons in the visible range.<sup>6</sup> In particular, the advances in IR sources, blue-, green-, and red-emitting colour phosphors are important in designing smart temperature-sensing devices and bio-imaging applications.<sup>7-9</sup> Y<sub>2</sub>Ti<sub>2</sub>O<sub>7</sub>, as one of the members of the classical pyrochlore family, has attracted much attention because of its unique optical properties and potential applications in up-conversion lasers, bio-imaging, and DNA detection.<sup>1-4,10,11</sup> However, the up-conversion efficiency (η) of these nano-crystals is still inadequate, thus limiting their wide applications. Moreover, various studies have been performed to enhance the up-conversion intensity η by changing the crystal phase, functionalising the surface of the sample, incorporating a co-dopant sensitizer, and/or by core-shell formation.<sup>12-15</sup> Moreover, the intensity of Ln<sup>3+</sup>-doped up-conversion materials strongly depends on intra 4f-4f transition probabilities and is also influenced by the crystal field symmetry and crystallinity of the samples.<sup>16,17</sup> Li<sup>+</sup> ions can be doped in the host matrices efficiently because of their small ionic radius, either by substitution or

interstitial. The substitution and/or interstitial incorporation of  $\text{Li}^+$  ions in the  $\text{Ln}^{3+}$ -doped host matrices distorts the lattice symmetry of the crystal field around the  $\text{Ln}^{3+}$  ions ( $\text{Er}^{3+}$  in our case), thus improving the up-conversion intensity.<sup>17,18</sup> Several studies have reported the improvements in up-conversion intensities for different host matrices by  $\text{Li}^+$  ion co-doping. *Chen et al.*<sup>19</sup> reported 25-fold improvement in the visible up-conversion intensity in  $\text{Y}_2\text{O}_3:\text{Er}^{3+}/\text{Yb}^{3+}/\text{Li}^+$ -doped nano-phosphors, while 30-fold improvement has been obtained after  $\text{Li}^+$  incorporation in  $\text{NaGdF}_4:\text{Er}^{3+}/\text{Yb}^{3+}$  host matrices.<sup>20</sup> *Bai et al.*<sup>21</sup> and *Li et al.*<sup>22</sup> also reported the effect of  $\text{Li}^+$  ions on the significant enhancement in up-conversion intensity and proposed the change in crystal symmetry around the  $\text{Ln}^{3+}$  ions as one of the reasons for luminescence enhancement.

In recent years, fluorescence-based temperature-sensing technique has attracted much attention and contributed a vital role because it can overcome the strong signal-to-noise ratio (SNR) and hazardous sparks, which are not possible in conventional temperature sensors such as thermocouple detectors in oil refineries and coal mines.<sup>23–25</sup> In conventional temperature sensors derived by the liquid and metal expansion principle, temperature is measured by the heat flow using an invasive probe. Optical temperature sensors are based on temperature-dependent fluorescence lifetimes and the fluorescence intensity ratio (FIR) of the thermally coupled electronic transitions of  $\text{Ln}^{3+}$  ions. These methods have attracted much attention and proved superior to the pre-existing conventional methods. The FIR technique based on the measurement of luminescence intensities from two thermally coupled levels of  $\text{Ln}^{3+}$  ions is independent of spectrum losses and fluctuations in the excitation intensity; therefore, it can be used to provide more accurate temperature measurements.<sup>26</sup> The operating temperature range and sensitivity should be high for a high-quality temperature sensor. The search for a new class of material for this purpose is challenging and still underway.

Herein, we report a structural, up-conversion, and temperature-sensing approach by introducing  $\text{Li}^+$  ions into  $\text{Y}_2\text{Ti}_2\text{O}_7:\text{Er}^{3+}/\text{Yb}^{3+}$  phosphor prepared by a conventional solid-state reaction method. The structures of the phosphors with different amounts of  $\text{Li}^+$  ion concentrations were analysed by X-ray diffraction (XRD), Fourier transform infrared (FTIR) spectroscopy, X-ray photoelectron spectroscopy (XPS), and field-emission scanning electron microscopy (FE-SEM). A substantial change in the up-conversion intensity and decay time ( $\tau$ ) of intermediate  $^4\text{S}_{3/2}$  (green band) state was monitored. The mechanism involved in the up-conversion process was elucidated by pump power dependence, suitable energy level diagram, and decay studies. To study the temperature-sensing behaviour, an FIR-based technique was used. To the best of our knowledge, no temperature-sensing studies have been conducted for the  $\text{Er}^{3+}/\text{Yb}^{3+}$  and  $\text{Li}^+$  tri-doped  $\text{Y}_2\text{Ti}_2\text{O}_7$  pyrochlore system. The thermally coupled  $^2\text{H}_{11/2}$  and  $^4\text{S}_{3/2}$  levels of  $\text{Er}^{3+}$  ions in the spectrum demonstrated temperature-dependant behaviour and probed for optical thermometry using the FIR technique.

## 2. Experimental

### 2.1 Sample Preparation

$\text{Er}_x\text{Yb}_y\text{Li}_z\text{Y}_{2-x-y-z}\text{Ti}_2\text{O}_7$  ( $x=1$  and  $y=2$  at%,  $z = 0, 2, 5, 7, 10$ , and 15 at%) samples were prepared by a conventional solid-state ceramic method. Analytical reagent (AR) grade yttrium oxide ( $\text{Y}_2\text{O}_3$ , Alfa Aesar, 99.99%), titanium oxide ( $\text{TiO}_2$ , 99.9%, Alfa Aesar), ytterbium oxide ( $\text{Yb}_2\text{O}_3$ , Alfa Aesar, 99.99%), erbium oxide ( $\text{Er}_2\text{O}_3$ , Alfa Aesar, 99.98%) and lithium carbonate ( $\text{Li}_2\text{CO}_3$ , Merck, 99.98%) were used as the starting materials. Stoichiometric amounts of starting materials were mixed in a planetary ball mill with zirconia jars and zirconia balls for 6 h at 50 rpm using acetone as the mixing medium (solvent). The dried mixed powders were calcined in an alumina crucible in ambient atmosphere (air) at 1200 °C for 6 h, and then the samples were furnace cooled to room temperature. A few drops of a 2% solution of polyvinyl alcohol (PVA) were added to the powder as the binder. The calcined powders were ground, mixed, and pelletized at 75 kN. The pellets were sintered at 1300 °C for 12 h. During the sintering, the pellets were initially heated at a rate of 2 °C per min to 500 °C and then kept at this temperature for 1 h to evaporate the binder. Then, the pellets were heated at a rate of 4 °C per min to the sintering temperature of 1300 °C. After sintering, the samples were furnace cooled to room temperature.

### 2.2 Characterization techniques

The structure of the phosphor was identified by XRD using a Rigaku miniflex-II diffractometer and  $\text{Cu}_{K\alpha}$  radiation (1.5406 Å) at ~30 kV and 15 mA. All the patterns were recorded from 20 to 90° with a step size of 0.02°. The FTIR spectra of the samples were recorded using a Shimadzu spectrophotometer in the range 4000–400  $\text{cm}^{-1}$ . The sample was mixed with KBr (Sigma Aldrich, 99.99%) in a 1:5 ratio, and a transparent pellet was prepared. Micro-Raman spectra have been recorded under 514.5 nm  $\text{Ar}^+$  excitation at room temperature. The chemical composition and valence state of the elements were analysed by XPS using a monochromatic  $\text{Al}_{K\alpha}$  ( $h\nu = 1486.6\text{eV}$ ) X-ray source and a hemispherical analyzer (SPECS, HSA3500). The recorded spectra were charge-corrected to the  $\text{C}1s$  ~284.6 eV as the reference. The morphology of the synthesised samples were examined by FE-SEM, model JEOL JSM-6700 (Japan). Osmium was coated by spraying it on the sample surfaces using a Hitachi (Japan) fine coat ion sputter E-1010 unit. To avoid the expected charging of the specimens, the coating was performed each time before the FE-SEM observation. The up-conversion emission spectra were recorded using a Princeton triple-grating turret monochromator (Acton SP-2300) equipped with a photomultiplier tube (PMT) and a personal computer (PC). The samples were irradiated using a 976 nm (CW) laser at different laser powers (i.e., 0.3 to 2.4 W) with a spot size of ~1.4 mm. For the up-conversion at different temperatures, the laser beam was focused at the edge of the pellet samples, and a thermocouple was placed close to the focal spot. Also for the study of FIR variation with laser power density, the upconversion (UC) spectra of the phosphors have been recorded at different excitation power densities at room temperature. Lifetime decay ( $\tau$ ) measurements were carried out by chopping the ~976 nm laser beam with a mechanical chopper and using a quick start digital oscilloscope.

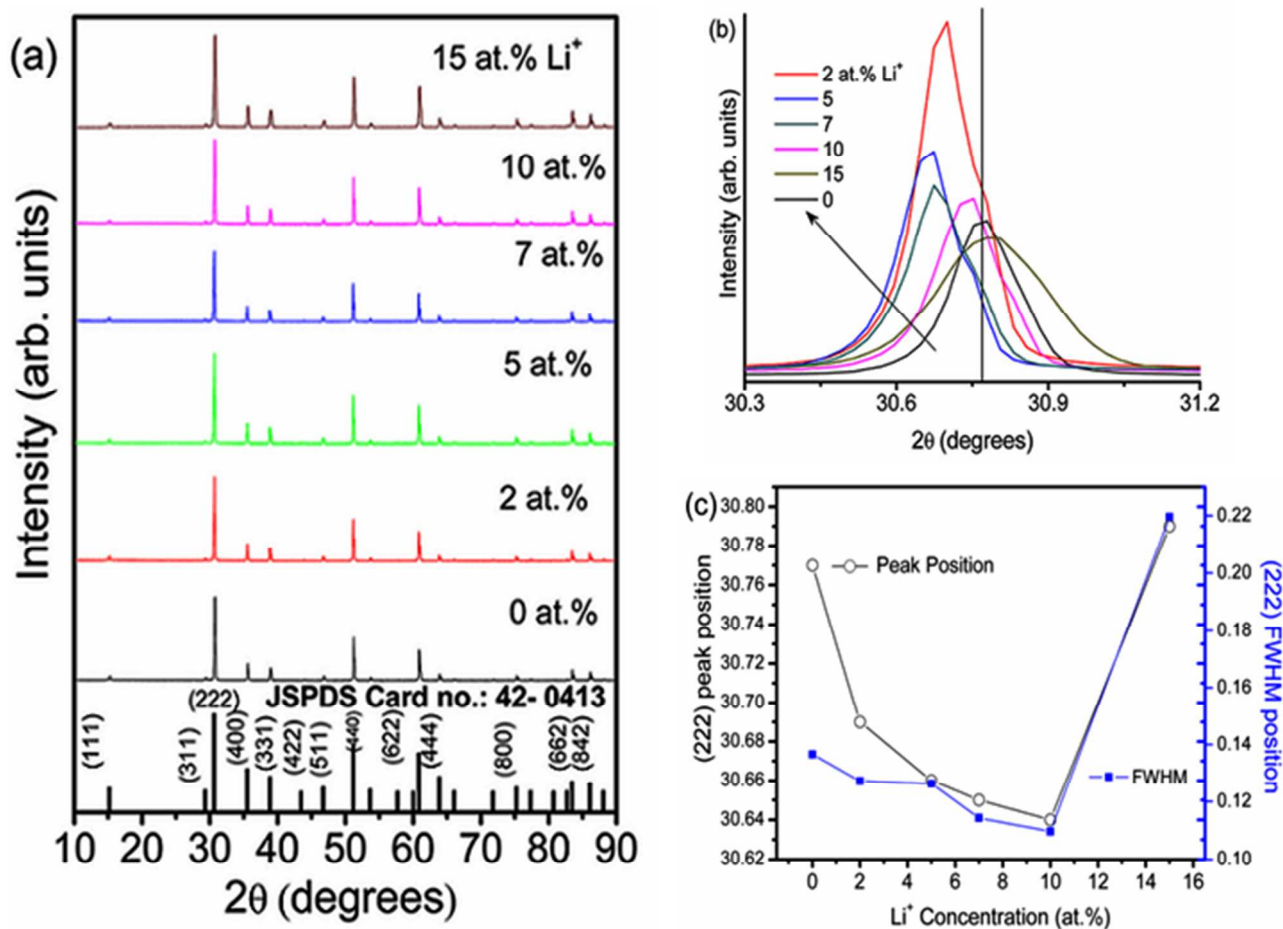


Fig. 1 XRD pattern of (a) Er<sup>3+</sup>/Yb<sup>3+</sup>-doped Y<sub>2</sub>Ti<sub>2</sub>O<sub>7</sub> and Li<sup>+</sup> (2, 5, 7, 10, and 15 at%) co-doped Y<sub>2</sub>Ti<sub>2</sub>O<sub>7</sub>, (b) shifting of (222) peak with Li<sup>+</sup> ion concentration, and (c) change in peak position and FWHM of (222) peak in 2θ.

### 3. Results and discussion

#### 3.1 Structural Analysis

##### 3.1.1 XRD Analysis

The XRD patterns of Y<sub>2</sub>Ti<sub>2</sub>O<sub>7</sub>:Er<sup>3+</sup>/Yb<sup>3+</sup> (EYYTO) co-doped with Li<sup>+</sup> (0, 2, 5, 7, 10, and 15 at%) ions are shown in Fig. 1. All the observed intensity patterns of Li<sup>+</sup> co-doped samples matched well with typical face centred cubic pyrochlore (JCPDS card no. 42-0413).<sup>11</sup> The co-doping of Li<sup>+</sup> ions did not produce any other impurity phase in Y<sub>2</sub>Ti<sub>2</sub>O<sub>7</sub> (YTO) system. The expansion of main diffraction peak (222) for all Li<sup>+</sup> (0, 2, 5, 7, 10, and 15 at%) co-doped samples is shown in Fig. 1(b).

The peak position corresponding to (222) shifted to a lower angle (2θ) side up to 10 at% Li<sup>+</sup>, and it shifted to a higher angle side for 15 at% Li<sup>+</sup>. The peak position of the diffraction peak (222) and full width at half maximum (FWHM) for different Li<sup>+</sup> concentrations are shown in Fig. 1(c). The shifting of main diffraction peak position indicates that Li<sup>+</sup> ions can be occupied in both ways either via substitution or entering into interstitial sites of host matrices. Because the effective ionic radii of Li<sup>+</sup>, Er<sup>3+</sup>, Yb<sup>3+</sup>, and Y<sup>3+</sup> are ~0.76, 0.89, 0.985, and 0.9 Å, respectively,<sup>27</sup> there is a debate on Li<sup>+</sup> co-doped systems: on Li<sup>+</sup> doping, whether Li<sup>+</sup> ions can be substituted and/or incorporated into interstitial sites. *Parchur et al.* reported that YPO<sub>4</sub>:Eu unit cell volume was

significantly enhanced by Li<sup>+</sup> co-doping. Moreover, the shifting of main diffraction peaks towards lower angle side (2θ) demonstrates that Li<sup>+</sup> ions were incorporated into interstitial sites.<sup>18</sup> We have not observed any other phases upto 15 at% doped Li<sup>+</sup> into EYYTO samples. The intensity of diffraction patterns increased up to 2 at% Li<sup>+</sup> co-doping and then decreased, indicating the association of surface defects on the surface of the samples. To understand the structural changes, Rietveld analysis was performed on the XRD data using the *FullProf* software.<sup>28</sup> The peak profiles were modelled using Pseudo-Voigt function and the background was described in terms of a six-coefficient polynomial. The *R<sub>wp</sub>* (weighted-pattern factor) and *S* (goodness-of-fit) parameters were used as the numerical criteria for the quality of the calculated fit to the experimental diffraction data. In Y<sub>2</sub>Ti<sub>2</sub>O<sub>7</sub>, there are four different crystallographic axes, namely, Y: (16d), Ti: (16c), O1 (48f), and O2 (8b) assuming that a Ti<sup>4+</sup> ion is situated at the origin of the unit cell. The Y and Ti sites have eight and six ion co-ordination sites, respectively, while the crystallographically different axes of oxygen O1 (48f) was co-ordinated to 2Ti and 2Y. O2 (8b) was co-ordinated to 4Y ions, while the third anionic site, O3 (8a), was co-ordinated to the 4Ti ions and generally found to be empty in ordered pyrochlore lattice.<sup>29,30</sup>

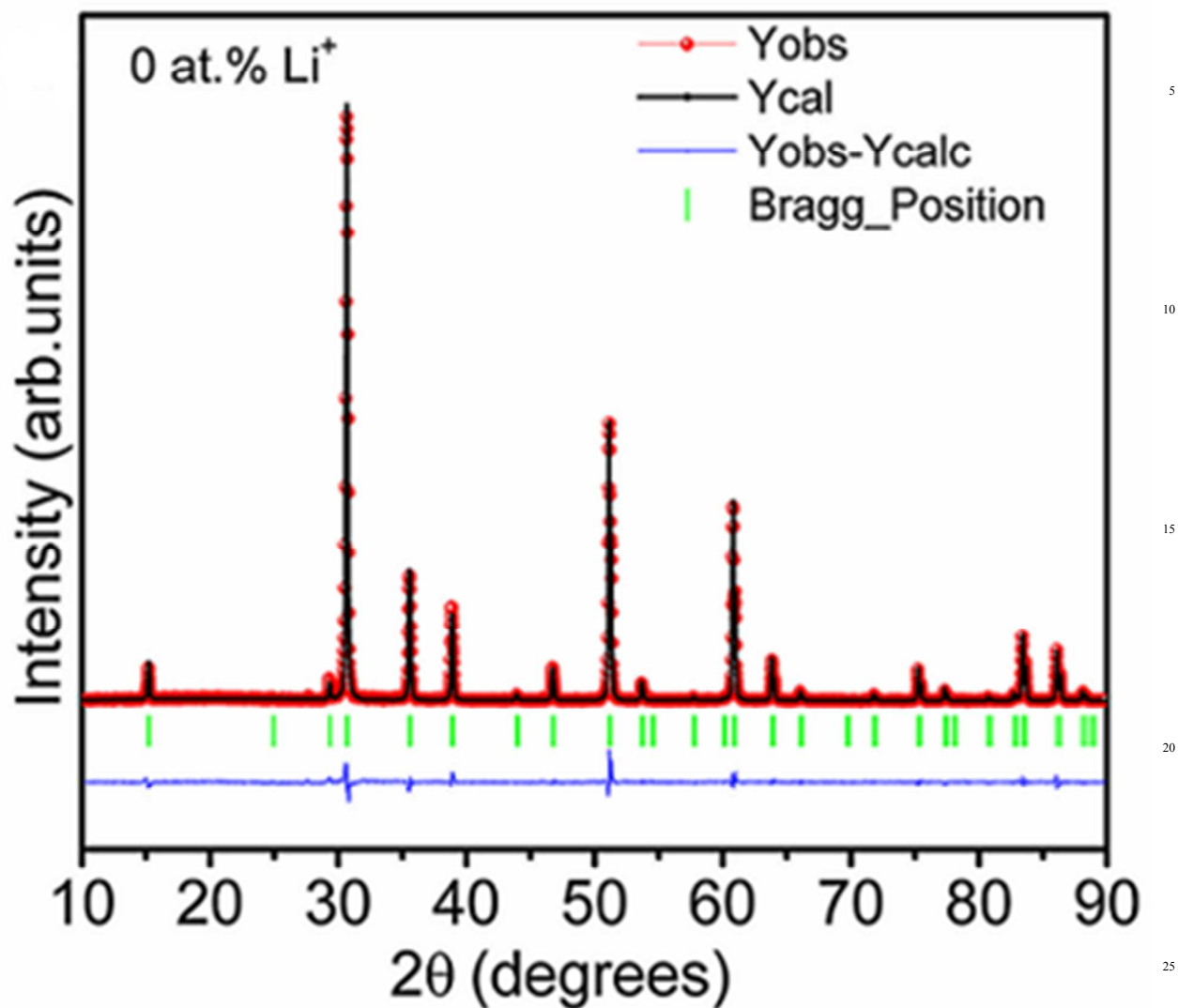


Fig. 2 Observed, calculated, and difference X-ray diffraction patterns for  $\text{Li}^+$  (0 at%) co-doped  $\text{Er}^{3+}/\text{Yb}^{3+}:\text{Y}_2\text{Ti}_2\text{O}_7$ .

Since change of peak in lower  $2\theta$  upon co-doping of 10 at.%,  $\text{Li}^+$  ions occupy interstitial sites or even grain boundary. However, we do not see  $\text{Li}_2\text{O}$  peaks. This may be due to very low atomic scattering of X-rays from  $\text{Li}^+$  ions, which is undetectable in our XRD instrument. There will be charge balance after  $\text{Li}^+$  co-doping in lattice and this can be compensated by introduction of oxygen vacancy or/and conversion of some  $\text{Ti}^{4+}$  ions to  $\text{Ti}^{3+}$  ions.<sup>31</sup> In this view, we analyse Rietveld plot for  $\text{Y}_2\text{T}_2\text{O}_7:\text{Er}^{3+}/\text{Yb}^{3+}$  ( $\text{Li} = 0$  at.%) (Shown in Fig. 2). The detail structures for Li-codoping samples can be solved by Neutron scattering technique, which will be done in future study.

Fig.2 shows the Rietveld refinement of the powder diffraction data of  $\text{Li}^+$  (0 at%) co-doped EYYTO. The Bragg reflections and the difference in observed and calculated intensities are shown in the figure. In the crystal structure, Y and Ti occupy the special positions with  $Fd3m$  space group (no. 227). Y and Ti atoms occupy the same crystallographic sites (16d and 16c Wyckoff positions). Further, Y is associated with eight ion co-ordination making  $\text{YO}_8$  polyhedral, while Ti has six ion co-

ordinations by forming  $\text{TiO}_6$  polyhedron. There are two types of oxygen atoms: O1(48f) and O2(8b). The refined parameters e.g., atoms/ions, Wyckoff positions, thermal parameters, and site occupancy and lattice parameters for  $\text{Li}^+$  free  $\text{Y}_2\text{T}_2\text{O}_7:\text{Er}^{3+}/\text{Yb}^{3+}$  sample is listed in Table S1 (ESI). There are two types of bond involvement in  $\text{YO}_8$  group, (Y–O1) and (Y–O2), while the  $\text{TiO}_6$  group showed only one type of bond (Ti–O1). The bond lengths of Y–O1 was found 2.512 Å, whereas the bond length of Y–O2 was ~2.185 Å for  $\text{Li}^+$  free sample. Selected bond distances and coordination numbers of  $\text{Li}^+$  free  $\text{Y}_2\text{T}_2\text{O}_7:\text{Er}^{3+}/\text{Yb}^{3+}$  obtained from the Rietveld refinement are listed in Table S2(ESI).

### 3.1.2 XPS Study

To investigate the chemical composition of material surface, a well-known, extensively used X-ray photon spectroscopy (XPS) technique was used. All the obtained XPS data of elements were charge corrected with respect to C 1s, which appeared at ~284.6 eV; it arises mainly because of the presence of adventitious carbon during atmospheric exposure. The survey scan of core

binding energy (BE) of Y, Ti, O, Er, Yb, and Li in the range 0–1100 eV is shown in Fig.S1 (ESI). Figs. 3(a) (i)–(vi) show the XPS spectra of Y ( $3d$ ) for 0, 2, 5, 7, 10, and 15 at%  $\text{Li}^+$  co-doped EYYTO samples obtained in the range 153–162 eV. For  $\text{Li}^+$ -free EYYTO samples, the peak corresponding to Y( $3d$ ) had a core BE of  $\sim 156.85$  eV ( $3d_{5/2}$ ) and  $158.92$  eV ( $3d_{3/2}$ ) and a FWHM of  $\sim 2.2$  and  $2.3$  eV. On increasing  $\text{Li}^+$  (2, 5, 7, 10, and 15 at%) co-doping concentration, there was a slight change in BE ( $\pm 0.63$  eV) and FWHM ( $\pm 0.3$  eV) corresponding to  $\text{Y}3d_{5/2}$  peak towards higher eV within the limits of error bar. Moreover, a very nominal change in BE ( $\pm 0.59$  eV) and FWHM ( $\pm 0.5$  eV) corresponding to  $\text{Y}3d_{3/2}$  peak was observed. These results confirm the +3 formal oxidation state of Y.<sup>32</sup> Moreover, the integrated intensity ratio of ( $3d_{5/2}$ ) to ( $3d_{3/2}$ ) was found to be  $\sim 1.64, 2.89, 1.54, 0.85, 1.79,$  and  $\sim 1.74$  for 0, 2, 5, 7, 10, and 15 at%  $\text{Li}^+$  co-doping, respectively.

The XPS spectra of the core BE of  $\text{Ti}2p_{3/2}$  and  $\text{Ti}2p_{1/2}$  regions (between 455–467 eV) are shown in Fig. 3(b) (i)–(vi). It has been

reported in literature that Ti in its +4 oxidation state has BE values in the range  $\sim 458$ – $460$  eV for  $2p_{3/2}$  level.<sup>33</sup> Notably, diverse BE has been reported for  $\text{Ti}^{4+}$  ions. Hence, the energy separation between the O1s and BE of  $\text{Ti}(2p_{3/2})$  was investigated. To investigate the chemical composition of material surface, a well-known, extensively used X-ray photon spectroscopy (XPS) technique was used. All the obtained XPS data of elements were charge corrected with respect to C 1s, which appeared at  $\sim 284.6$  eV; it arises mainly because of the presence of adventitious carbon during atmospheric exposure. The survey scan of core binding energy (BE) of Y, Ti, O, Er, Yb, and Li in the range 0–1100 eV is shown in Fig.S1 (ESI). Figs. 3(a) (i)–(vi) show the XPS spectra of Y ( $3d$ ) for 0, 2, 5, 7, 10, and 15 at%  $\text{Li}^+$  co-doped EYYTO samples obtained in the range 153–162 eV. For  $\text{Li}^+$ -free EYYTO samples, the peak corresponding to Y( $3d$ ) had a core BE of  $\sim 156.85$  eV ( $3d_{5/2}$ ) and  $158.92$  eV ( $3d_{3/2}$ ) and a FWHM of  $\sim 2.2$  and  $2.3$  eV. On increasing  $\text{Li}^+$  (2, 5, 7, 10, and 15 at%) co-doping concentration, there was a slight change in BE ( $\pm 0.63$  eV) and

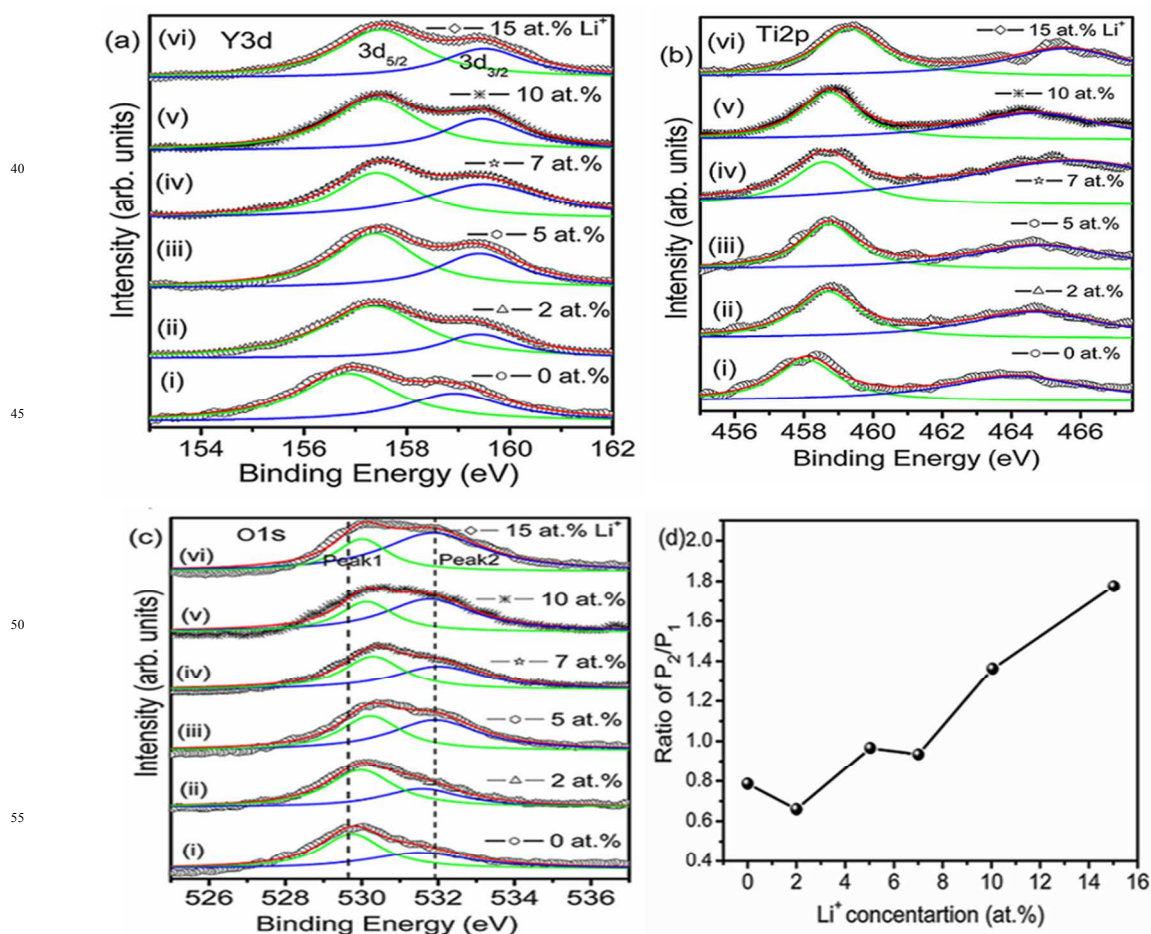


**Fig. 3** XPS spectra of (a) Y ( $3d$ ), (b) Ti ( $2p$ ), and (c) O ( $1s$ ) of  $\text{Li}^+$  co-doped  $\text{Y}_2\text{Ti}_2\text{O}_7:\text{Er}^{3+}/\text{Yb}^{3+}$  (at% of  $\text{Li}^+$  ion is shown in the figure). (d) Ratio of deconvoluted peak positions with respect to  $\text{Li}^+$  concentration.

FWHM ( $\pm 0.3$  eV) corresponding to  $\text{Y}3d_{5/2}$  peak towards higher eV within the limits of error bar. Moreover, a very nominal change in BE ( $\pm 0.59$  eV) and FWHM ( $\pm 0.5$  eV) corresponding to  $\text{Y}3d_{3/2}$  peak was observed. These results confirm the +3 formal oxidation state of Y.<sup>32</sup> Moreover, the integrated intensity ratio of ( $3d_{5/2}$ ) to ( $3d_{3/2}$ ) was found to be  $\sim 1.64, 2.89, 1.54, 0.85, 1.79,$  and

$\sim 1.74$  for 0, 2, 5, 7, 10, and 15 at%  $\text{Li}^+$  co-doping, respectively.

The XPS spectra of the core BE of  $\text{Ti}2p_{3/2}$  and  $\text{Ti}2p_{1/2}$  regions (between 455–467 eV) are shown in Fig. 3(b) (i)–(vi). It has been reported in literature that Ti in its +4 oxidation state has BE values in the range  $\sim 458$ – $460$  eV for  $2p_{3/2}$  level.<sup>33</sup> Notably, diverse BE has been reported for  $\text{Ti}^{4+}$  ions. Hence, the energy separation

between the O1s and BE of Ti(2p<sub>3/2</sub>) was investigated to determine the valence state of Ti ions. The energy separation, i.e., (O1s-2p<sub>3/2</sub>), was found to be in the range  $71.3 \pm 0.35$ , demonstrating +4 oxidation state in EYYTO sample. Christopher *et al.*<sup>34</sup> reported the XPS study of titanates; the peak at  $\sim 464.1$  eV was attributed to the core BE of Ti (2p<sub>1/2</sub>). Moreover, they also mentioned some satellite peaks at 462.2 and 469.7 eV for 2p<sub>3/2</sub> and 2p<sub>1/2</sub> levels, respectively. The typical XPS spectra showing the core BE and intensity of Er(4d), Yb(4d), and Li(1s) with Li<sup>+</sup> concentration are shown in Figs. S1(b)–(d) (ESI); their profile peaks matched well with those reported in literature.<sup>33, 35, 36</sup> Because of the lower concentration of Er<sup>3+</sup>, Yb<sup>3+</sup>, and Li<sup>+</sup> present in the sample, a comparatively low intensity was observed. The XPS spectra of O1s are used as a probe for investigating the presence of oxygen ion vacancies on the surface of a sample. The peaks were de-convoluted using Lorentzian function. In the case of Li<sup>+</sup>-free EYYTO sample, the two peaks well fitted to BE  $\sim 529.7$  (P<sub>1</sub>) and 531.5 eV (P<sub>2</sub>) with FWHM  $\sim 1.8$  and 3.2 eV, respectively. On increasing Li<sup>+</sup> co-doping, the peak position slightly changed from  $\pm 0.08$  to 0.5 eV (Fig.3(c)). On Li<sup>+</sup> co-doping, all the peaks showed asymmetric behaviour towards higher BE. Moreover, the two peaks, further attributed to the presence of two non-equivalent crystallographic sites, were present in the typical pyrochlore system (A<sub>2</sub>B<sub>2</sub>O<sub>6</sub>O'). Further, the relative area of the P<sub>2</sub>/P<sub>1</sub> ratio of Li<sup>+</sup> (0, 2, 5, 7, 10, and 15 at%) EYYTO samples provided an interesting feature, as shown in Fig. 3(d). The ratio of P<sub>2</sub>/P<sub>1</sub> decreased for 2 at% Li<sup>+</sup> compared to Li<sup>+</sup>-free sample, and it shows an increasing trend for higher at% of Li<sup>+</sup> concentration. This is probably because of the creation of oxygen ion vacancies and/or surface defects through the sample surface with the introduction of Li<sup>+</sup> ions into the host matrix.<sup>36</sup>

### 3.1.3 FTIR Studies

Fig.4 (a-f) show the FT-IR spectra of Li<sup>+</sup> (0, 2, 5, 7, 10, and 15 at%) co-doped Y<sub>2</sub>Ti<sub>2</sub>O<sub>7</sub>:Er<sup>3+</sup>/Yb<sup>3+</sup>. The phonon cut-off energy bands at 417 cm<sup>-1</sup> (Y–O1), 463 cm<sup>-1</sup> (Y–O2), and at 573 cm<sup>-1</sup> (Ti–O1) were almost identical for the samples, dictating the lattice vibrational mode; thus, the multi-phonon non-radiative decay channel was not altered by further doping of Li<sup>+</sup> ions. Moreover, the formation of pure phase Y<sub>2</sub>Ti<sub>2</sub>O<sub>7</sub>:Er<sup>3+</sup>/Yb<sup>3+</sup> and Li<sup>+</sup> (2, 5, 7, 10, and 15 at%) co-doped Y<sub>2</sub>Ti<sub>2</sub>O<sub>7</sub>:Er<sup>3+</sup>/Yb<sup>3+</sup> phosphors was supported by FTIR analysis.<sup>11</sup>

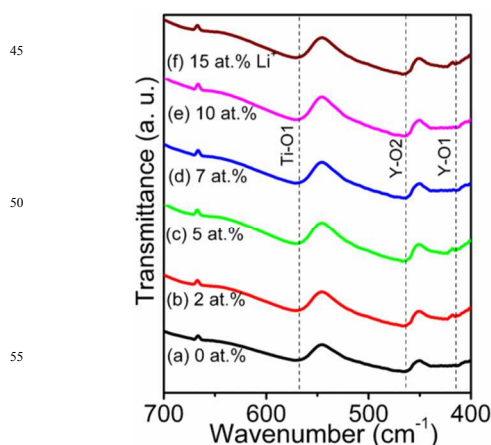


Fig. 4 Measured FT-IR transmission spectra of Y<sub>2</sub>Ti<sub>2</sub>O<sub>7</sub>:Yb<sup>3+</sup>/Er<sup>3+</sup>/Li<sup>+</sup> co-doped phosphors: (a) 0 at%, (b) 2 at%, (c) 5 at%, (d) 7 at%, (e) 10 at%, and (f) 15 at% Li<sup>+</sup> ion.

### 3.1.4 Raman Analysis

Fig. 5 (a) shows the Raman spectra of Li<sup>+</sup> (0, 2, 5, 7, 10, and 15 at%) co-doped Y<sub>2</sub>Ti<sub>2</sub>O<sub>7</sub>. Raman technique is more sensitive to metal-oxygen vibrational modes and hence probed for the local disorder present in the lattice. Because pyrochlore can be seen as a superstructure of fluorite induced by the ordering of A and B cations into nonequivalent crystallographic sites and the ordering of anions into three sites 48f, 8a, and 8b the latter remaining empty in a perfectly ordered lattice, a brief description of pyrochlore and fluorite Raman activity is relevant. In a perfect AO<sub>2</sub> fluorite (*Fm*3*m* space group, *Z* = 4), only one mode (T<sub>2g</sub>) is expected, which involves oxygen vibration in the tetrahedral cage formed by four A cations. In A<sub>2</sub>B<sub>2</sub>O<sub>7</sub> pyrochlores (*Fd*3*m*, *Z* = 8) there are six Raman active modes (A<sub>1g</sub>, E<sub>g</sub>, 4T<sub>2g</sub>), involving only vibrations of oxygens at both 48f and 8a sites.<sup>37</sup> According to group theory irreducible representation Raman spectra revealing pyrochlore structures having six Raman active modes represented as  $\Gamma = A_{1g} + E_g + E_{2g}$ , where symbols represent irreducible group representation. The active Raman bands were A<sub>1g</sub>, E<sub>g</sub> and 4T<sub>2g</sub> while IR active is 7F<sub>1u</sub>.<sup>38</sup> Sanjuan *et al.*<sup>37</sup> explained the characteristic modes of YTO pyrochlore observed at 310 cm<sup>-1</sup> which has the contributions from E<sub>g</sub> and T<sub>2g</sub> modes both. The bands at 515 and 711 cm<sup>-1</sup> correspond to A<sub>1g</sub> mode of vibration

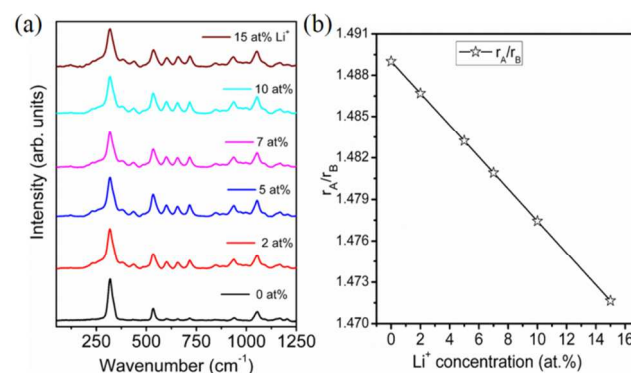


Fig.5 (a) Raman spectra of Li<sup>+</sup> (0, 2, 5, 7, 10 and 15 at.%) co-doped EYYTO and (b) variation of cationic radius ratios ( $r_A/r_B$ ) vs Li<sup>+</sup> ion concentrations.

and one of the T<sub>2g</sub> mode of vibration, respectively. The A<sub>1g</sub> frequency mode provides information about the force constant of Y<sub>2</sub>Ti<sub>2</sub>O<sub>7</sub> pyrochlore. The vibration of the TiO<sub>6</sub> octahedron is responsible for the A<sub>1g</sub> mode of vibration of Y<sub>2</sub>Ti<sub>2</sub>O<sub>7</sub> pyrochlore structure. The major contribution for this mode is mainly due to force constants associated with O–Ti–O bending.<sup>37</sup> Recently, Camacho *et al.*<sup>39</sup> studied the Raman spectra of Er<sup>3+</sup>/Yb<sup>3+</sup> doped hybrid materials and reported that the band situated near 368 cm<sup>-1</sup> is the metal oxygen (Yb–O) similar to the band at 377 (here 381 cm<sup>-1</sup>) of (Y–O) stretching vibration, while characteristic peaks of Er–O are found in the range of 500–580 cm<sup>-1</sup> and also some small traces of Raman bands near 620–680 cm<sup>-1</sup> and 780–900 cm<sup>-1</sup> are observed. Vibrational modes observed are most pronounced for 2 at% of Li<sup>+</sup> indicating the best crystallinity and hence the best atomic ordering. It has been worthwhile to mention that after Li<sup>+</sup> co-doping, a slight broadening at 310 cm<sup>-1</sup>

in the Raman spectra occurs (Shown in Fig. 5). Notably, pyrochlore structure bands have been observed for  $\text{Li}^+$  doped EYYTO samples. It also rules out the phase segregation/change from YTO matrices.

Also some additional Raman bands having weak intensity have been observed and these are related to the presence of the vacancies, defects, and foreign ions in the ordered lattice which disrupts the translational symmetry (i.e.  $k = 0$  selection rule is relaxed). Phonons having all parts of the Brillouin zone contributed to the optical spectra, thereby resulting in Broad bands. Tyagi and his co-workers have reported the  $\text{Dy}^{3+}$  substituted  $\text{Sm}_2\text{Zr}_2\text{O}_7$  and reported the broadening in the Raman spectra after the  $\text{Dy}^{3+}$  substitution.<sup>40</sup> Even a very broad peak was observed upon heavy doping of  $\text{Dy}^{3+}$ . However it is not happen in our study upon doping of 15 at%  $\text{Li}^+$ . Still peaks corresponding Raman bands are sharp. It means that  $\text{Li}^+$  ions do affect pyrochlore structure. Most  $\text{Li}^+$  ions occupy either interstitial sites or grain boundary, which is predicted by XRD study. Even, if  $\text{Li}_2\text{O}$  is present in particles, it should be seen in Raman spectra.

### 3.1.5 SEM Studies

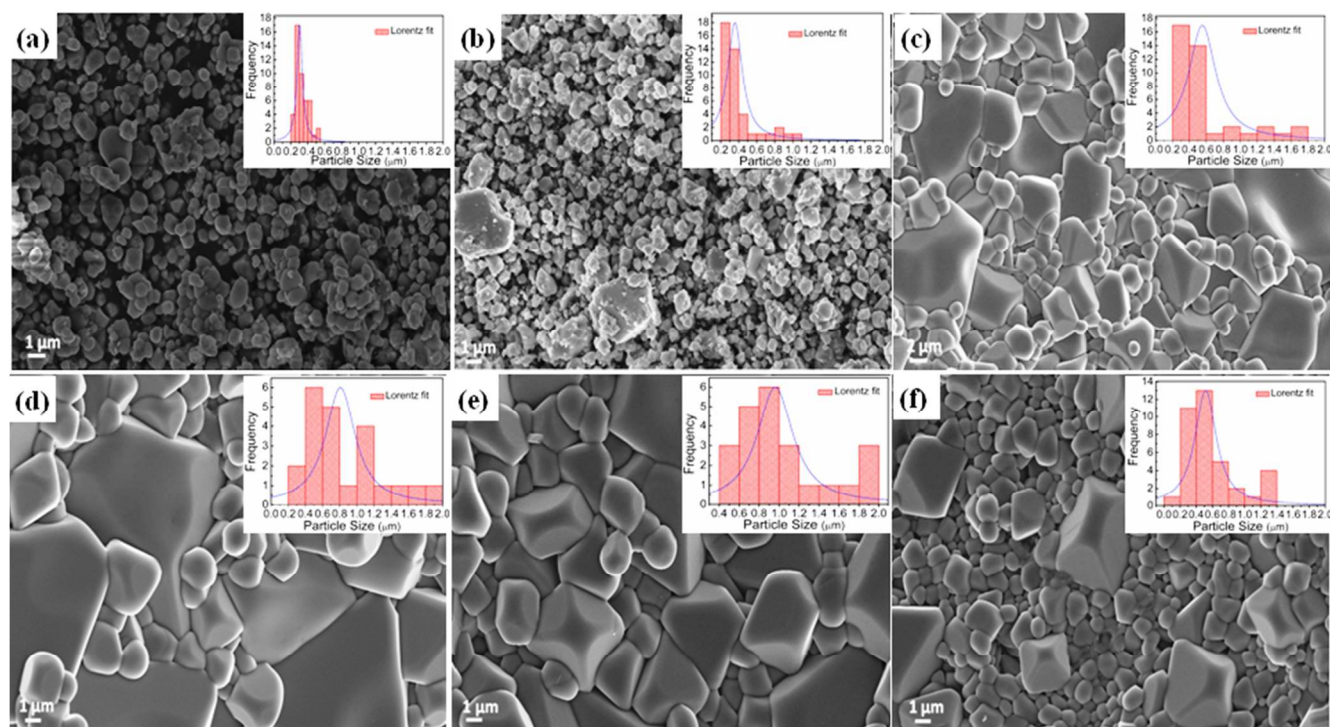


Fig. 6 FE- SEM micrographs of  $\text{Li}^+$  co-doped  $\text{Y}_2\text{Ti}_2\text{O}_7:\text{Er}^{3+}/\text{Yb}^{3+}$  (a)  $\text{Li}^+$  free, (b) 2 at%, (c) 5 at%, (d) 7 at%, (e) 10 at%, and (f) 15 at%  $\text{Li}^+$ . The insets of figures show the histograms of the average particle size distribution.

Fig. 6(a) shows the FESEM image of  $\text{Y}_2\text{Ti}_2\text{O}_7:\text{Er}^{3+}/\text{Yb}^{3+}$ , and the other images (Figs. 6(b)–(f)) represent the morphology of  $\text{Li}^+$  (2, 5, 7, 10, and 15 at.%) co-doped EYYTO. Prominent modification of the microstructure was observed from the micrographs of the  $\text{Li}^+$ -free EYYTO sample corroborates an inhomogeneous uneven morphology. As far as  $\text{Li}^+$  co-doped EYYTO samples is concerned, 2 at% of  $\text{Li}^+$  sample showed the highest roughness than higher concentrations of  $\text{Li}^+$ . This

Pure  $\text{Li}_2\text{O}$  crystallizes in the anti-fluoride structure and it gives only one allowed Raman band at  $523\text{ cm}^{-1}$ .<sup>41</sup> This peak is merged with the allowed transition of Raman band of  $\text{Y}_2\text{Ti}_2\text{O}_7$  pyrochlore. Thus, we could not distinguish the presence of  $\text{Li}_2\text{O}$  compound even if it is present.

Moreover for the completely ordered pyrochlore ( $\text{A}_2\text{B}_2\text{O}_7$ ), phase stability of the superstructure is predominantly determined by cationic radius ratio of the site A and B. It has been well documented in the literature that the pyrochlore lattice is supported by a radius ratio,  $r_A/r_B$ . The value of cationic radius ratios varies and lying between 1.46 and 1.78 for ordered pyrochlore structure.<sup>40</sup> Variation of radius ratio with  $\text{Er}^{3+}/\text{Yb}^{3+}/\text{Li}^+$  co-doped YTO has been performed and its values varies with the  $\text{Li}^+$  concentration and its lying in between 1.49 to 1.47 (shown in Fig. 5(b), which dictates the ordered pyrochlore solid solution structure.

indicates that the absorption of input light photons increases with increasing roughness of the sample; thus, the highest emission intensity was observed. Fan *et al.*<sup>42</sup> and Sun *et al.*<sup>43</sup> also proposed that the increased roughness and crystallinity of materials, in the presence of  $\text{Li}^+$  doping, are among one of the significant reasons for the enhancement in the luminescence intensity of lanthanides. However, further incorporation of  $\text{Li}^+$  ions in the samples decreased the crystallinity, and the morphology became irregular

(as shown in Figs. 6(c)–(f)) with defects induced on the sample surface. The micro-structural properties of the samples play a vital role for PL characteristics, because of the better crystallinity of the host–activator system transferring energy efficiently from the host to the activator, which was further confirmed by the respective PL spectra. Particles exhibit an irregular morphology because of the inherent characteristics of the used solid-state reaction method. Figs. 6(c), (d), (e), and (f) show that the particles almost have polyhedron morphology. From the SEM micrographs, it is evident that the particle size evolution is in the order of micron. For 15 at% co-doped sample, more uniform spherical microspheres of average diameter in the range ~0.5–1.5  $\mu\text{m}$  than rough cube-like structures were observed. Moreover, the percentage of rough cube-like structures first increased with  $\text{Li}^+$  co-doping up to 10 at% and then decreased. This is also supported by the XRD peak broadening (Fig. 1(b)). The histograms of the average particle size distribution of the particles are shown in the figures.

## 4. Optical Studies

### 4.1 Photoluminescence Studies

The up-conversion properties of  $\text{Li}^+$  (0, 2, 5, 7, 10, and 15 at%) co-doped EYYTO were studied at room temperature under ~976 nm excitation. The variation in up-conversion emission intensity versus  $\text{Li}^+$  concentration upon ~976 nm laser excitation is shown in Fig. 7. The up-conversion intensities show brilliant green emission followed by red emission. Two prominent bands were observed because of the up-conversion at ~524 and 548 nm, which are responsible for the green emission in the range 500–600 nm with the maximum intensity at ~548 nm. These two bands can be attributed to the  $^2\text{H}_{11/2} \rightarrow ^4\text{I}_{15/2}$  and  $^4\text{S}_{3/2} \rightarrow ^4\text{I}_{15/2}$  electronic transitions of  $\text{Er}^{3+}$  ion, respectively. Moreover, the band observed in the range 600–700 nm with the maximum intensity at ~661 nm was assigned to the  $^4\text{F}_{9/2} \rightarrow ^4\text{I}_{15/2}$  transition of  $\text{Er}^{3+}$ .

Moreover, the peaks at ~380, 410, and 487 nm in the near-UV and blue regions of the spectrum with a low intensity is well described in the inset of Fig. 7(a) (i) in the range 380–500 nm. These bands can be attributed to the electronic transitions, namely, the  $^4\text{G}_{11/2} \rightarrow ^4\text{I}_{15/2}$ ,  $^2\text{H}_{9/2} \rightarrow ^4\text{I}_{15/2}$ , and  $^4\text{F}_{5/2} \rightarrow ^4\text{I}_{15/2}$  of  $\text{Er}^{3+}$  ion on 976 nm excitation. The inset (ii) of Fig. 7(a) in the range 750–900 nm, with a well-splitted Stark pattern of the  $^4\text{I}_{9/2} \rightarrow ^4\text{I}_{15/2}$  transition of  $\text{Er}^{3+}$  ion, demonstrating the highly crystalline nature of EYYTO phosphor.<sup>11</sup> The variation in up-conversion intensity was observed with  $\text{Li}^+$  concentration and found to be the maximum for 2 at%  $\text{Li}^+$  (as shown in Fig. 7(a)). This is probably because the 2 at%  $\text{Li}^+$ -doped EYYTO sample has the most asymmetric environment around  $\text{Er}^{3+}$  ion. For higher concentrations of  $\text{Li}^+$  (5, 7, 10, and 15 at%), the intensity decreased. This is because of a lower proportion of  $\text{Li}^+$  incorporation in host lattice, thus inducing a fast ET from the host to the  $\text{Er}^{3+}$  ion. This may create the vacancies that act as the sensitizer, mixing the charge-transfer states.  $\text{Li}^+$  addition increased the PL intensity by increasing the radiative transition probability. However, an increase in the  $\text{Li}^+$  concentration over a certain limit generates a significant amount of oxygen ion vacancies in the lattice. Consequently, the crystal lattice

collapses, and the luminescence intensity decreases.<sup>35</sup> The inset shows the digital photographs of the up-conversion luminescence of EYYTO:2Li under 976 nm excitation using a suitable filter. The fluorescence intensities of the green and red bands were measured, and enhancements of ~15 and 8 fold were observed for EYYTO:2Li, more than that of  $\text{Li}^+$  free EYYTO sample. The integral intensities of 524, 548, and 661 nm bands showed similar trends as  $\text{Li}^+$  concentrations, corroborating the same up-conversion pathways (Fig. 7 (b)). Clearly, the green and red up-converted intensities enhanced drastically with  $\text{Li}^+$  concentration. The incorporation of  $\text{Li}^+$  ions in both substitution and/or interstitial sites changed the crystal field and surrounding environment of  $\text{Er}^{3+}$  ions. It was also confirmed by the Rietveld refinement XRD studies of all the measured samples with  $\text{Li}^+$  concentrations. Moreover,  $\text{Li}^+$  incorporation may change the electron density.

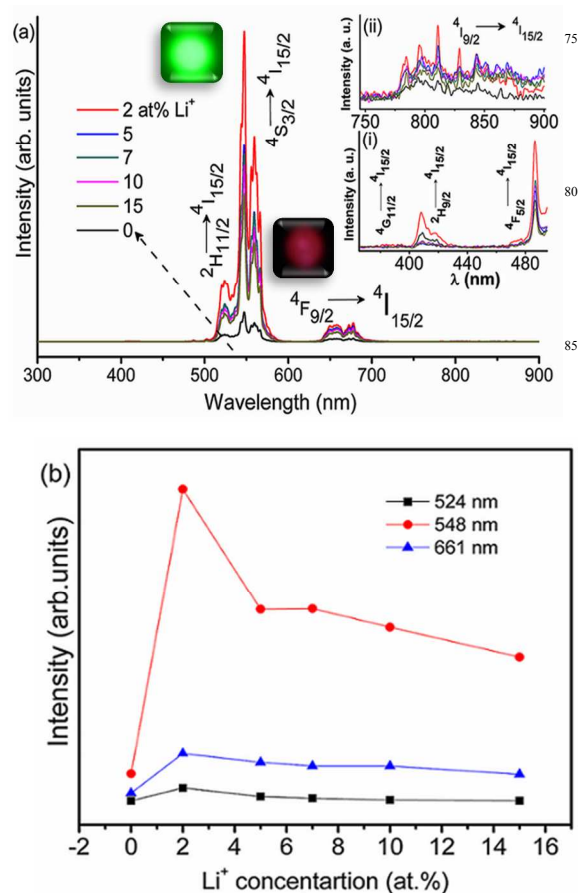


**Fig. 7** (a) Emission spectra of  $\text{Li}^+$  (0, 2, 5, 7, 10, and 15 at%) co-doped  $\text{Y}_2\text{Ti}_2\text{O}_7:\text{Er}^{3+}/\text{Yb}^{3+}$  phosphor under 976 nm excitation. Insets (i) and (ii) show the expansion in 380–500 nm and 750–900 nm. The digital photographs of EYYTO:2Li<sup>+</sup> were recorded using a Nikon Coolpix P500 digital camera using a suitable colour filters and (b) shows the integral intensity of green and red emissions as a function of the concentration of  $\text{Li}^+$  ions.

This change in environment around  $\text{Er}^{3+}$  may provide hypersensitive transitions with the selection rule as follows:  $|\Delta J| = 2$ ,  $|\Delta L| \leq 2$ , and  $|\Delta S| = 0$ , increasing the population density in the  $^4\text{S}_{3/2}$  state and opposing the cross-relaxation and energy back

transfer; thus, different folds of enhancement were observed for the green and red up-converted bands.<sup>17</sup> The enhanced up-conversion intensity indicates that the incorporation of different concentrations of  $\text{Li}^+$  ions can modify the local symmetry around  $\text{Er}^{3+}$  ions; a further enhancement in  $\text{Li}^+$  concentration decreased the up-conversion intensity.  $\text{Li}^+$  ions with smaller ionic radii can readily occupy and/or enter into the interstitial sites of the host by lowering the crystal field symmetry around  $\text{Er}^{3+}$  ions. Moreover, the incorporation of  $\text{Li}^+$  ions into host would create some defects, and oxygen ion vacancies associated with sample surfaces were also confirmed by the XPS study. The oxygen ion vacancies acted as the sensitizer for  $\text{Ln}^{3+}$  ions because of the overlapping of charge-transfer states; thus, enhanced PL was observed.<sup>44</sup> Moreover,  $\text{Li}^+$  incorporation may also improve the system crystallinity, lower the surface defects and non-radiative transitions; thus, an enhancement in up-conversion emission intensity was observed. To determine the number of up-converted photons involved in the up-conversion process, the up-conversion luminescence intensity of 2Li<sup>+</sup> co-doped EYYTO was measured as a function of pump power. The number of photons required for an unsaturated up-conversion process to populate the upper emitting levels can be well described as follows.<sup>45</sup>

$$I_{up} \propto I_{NIR}^n \quad (i)$$

where  $I_{up}$  is the up-conversion emission intensity,  $I_{NIR}$  is the pump laser intensity, and  $n$  is the number of pump photons required for up-conversion process.

The power dependence study of EYYTO:2Li sample is shown in Fig. 8. The slopes ( $n$  values) obtained from the linear fitting of the bi-log plots for ~524, 548, and 661 nm were ~2.2, 1.9, and 1.58, respectively, with slightly smaller values than the  $\text{Li}^+$ -free EYYTO sample. The obtained slope value confirmed that two-photon processes were involved in the observed green and red emissions for both the  $\text{Li}^+$ -doped and  $\text{Li}^+$ -free samples. Moreover, the power dependence was studied for the weak UV and blue bands, i.e., for ~380, 410, and 487 nm bands, and the slope values were found to be ~2.56, 2.87, and 2.7, i.e., three-photon processes were involved in these bands, as shown in Fig.S2 (†ESI). Because  $\text{Li}^+$  ions cannot absorb ~976 nm pump photon energy, ultimately, they are unable to transfer energy to  $\text{Er}^{3+}$  ion, which further confirms that the mechanism of the up-conversion was not affected by the incorporation of  $\text{Li}^+$  ions. Moreover, the slope values were altered slightly with  $\text{Li}^+$  ions, with smaller values for green and red emission bands than  $\text{Er}^{3+}/\text{Yb}^{3+}$ -doped  $\text{Y}_2\text{Ti}_2\text{O}_7$  bands.<sup>11,17</sup> Smaller  $n$  values demonstrated that the involved up-conversion process occurs comparatively easily to saturate  $\text{Li}^+$  co-doped EYYTO than the  $\text{Li}^+$ -free EYYTO samples. Moreover, EYYTO:2Li sample emitted green light at a low excitation power density of ~135  $\text{mWmm}^{-2}$  than EYYTO sample with an excitation power density of ~152  $\text{mWmm}^{-2}$  under 976 nm excitation, which may trigger photo-chemical reactions occurring in photodynamic therapy. Cheetham and co-workers reported the excitation power densities for ( $\text{Yb}^{3+}$ ,  $\text{Er}^{3+}$ , and  $\text{Tm}^{3+}$ ) and ( $\text{Er}^{3+}$  and  $\text{Yb}^{3+}$ ) doped  $\text{Y}_2\text{BaZnO}_5$  with the minimum excitation power of 25  $\text{mWmm}^{-2}$  and 90  $\text{mWmm}^{-2}$ , respectively.<sup>46</sup>

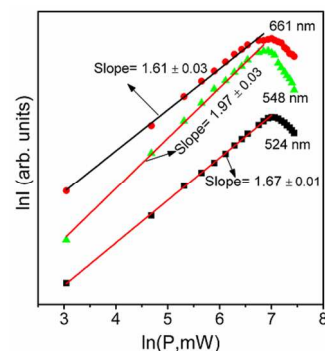


Fig. 8 Power dependence of green 524 ( $^2\text{H}_{11/2} \rightarrow ^4\text{I}_{15/2}$ ) and 548 nm ( $^4\text{S}_{3/2} \rightarrow ^4\text{I}_{15/2}$ ) and red emission 661 nm ( $^4\text{F}_{9/2} \rightarrow ^4\text{I}_{15/2}$ ) bands of 2 at%  $\text{Li}^+$  co-doped  $\text{Y}_2\text{Ti}_2\text{O}_7:\text{Yb}^{3+}/\text{Er}^{3+}$ .

## 4.2 Energy level diagram and energy transfer

On ~976 nm laser excitation,  $\text{Er}^{3+}$  and  $\text{Yb}^{3+}$  ions are promoted to their resonant excited states through ground-state absorption (GSA). Because  $\text{Er}^{3+}$  ions have a low absorption cross section, the GSA process was found to be weak for  $\text{Er}^{3+}$ .  $\text{Yb}^{3+}$  ions exhibit a nearly seven times higher absorption cross section ( $\sim 11.7 \times 10^{-21} \text{cm}^2$ ) than that of their  $\text{Er}^{3+}$  counterpart ( $\sim 1.7 \times 10^{-21} \text{cm}^2$ ). Thus, most of the impinging photon energy was absorbed by the  $\text{Yb}^{3+}$  ions and further transferred to  $\text{Er}^{3+}$  ions via different (ET) processes. The details of the different ET processes for the EYYTO:2Li system are shown in Fig. 9.

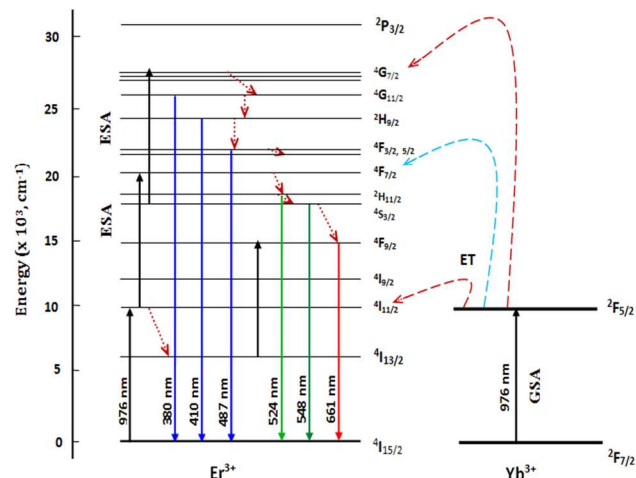


Fig. 9 Schematic partial energy level diagram and energy transfer processes involved in the up-conversion process.

## 4.3 Effect of temperature on up-conversion emission and temperature-sensing behaviour

To investigate the temperature-sensing behaviour of these phosphor (EYYTO:2Li) luminescence materials, the FIR technique was employed. In this technique, the fluorescence emitted from the thermally coupled closely spaced levels to a common final ground state is monitored, and the ratio of the emission intensities of these two bands is calculated as a function of temperature. In the case of  $\text{Er}^{3+}$  ions, the two levels,  $^2\text{H}_{11/2}$  and  $^4\text{S}_{3/2}$ , are closely spaced ( $\sim 500\text{--}600 \text{cm}^{-1}$ ) and thermally populated. The FIR of  $^2\text{H}_{11/2}$  and  $^4\text{S}_{3/2}$  levels to the ground state (i.e.,  $^4\text{I}_{15/2}$ ) of  $\text{Er}^{3+}$  level was applied to study the temperature-sensing behaviour in the temperature range 298–673 K at an excitation power of ~250 mW. Fig. 10(a) shows the green up-

conversion spectra of  $2\text{Li}^+$  co-doped EYYTO in the wavelength range 510–580 nm at the measured temperatures of 298 and 673 K. The peak positions of the green up-conversion bands ( ${}^2\text{H}_{11/2}$  and  ${}^4\text{S}_{3/2}$  levels) did not change; however, the corresponding intensities of these two bands centred at 524 nm and 548 nm varied substantially with the increase in the sample temperature. The fluorescence intensity of the green band centred at 524 nm ( ${}^2\text{H}_{11/2}$ ) is very low compared to the band centred at 548 nm at room temperature (298 K), while at the elevated temperature (673 K), the reverse trend was observed. Thus, the variation in the fluorescence intensity of the two peaks was estimated. According to Maxwell Boltzmann distribution, the photon population density of ions in the two thermally populated levels of  $\text{Er}^{3+}$ , i.e., for  ${}^2\text{H}_{11/2}$  and  ${}^4\text{S}_{3/2}$  can be expressed as follows:<sup>25, 48</sup>

$$\frac{n_H}{n_S} = \frac{g_H}{g_S} \exp\left(-\frac{E_H - E_S}{KT}\right) = \frac{g_H}{g_S} \exp\left(-\frac{\Delta E}{kT}\right) \quad (\text{ii})$$

where  $n_H$ ,  $n_S$ ,  $g_H$ , and  $g_S$  are the corresponding particle densities and degeneracy factors associated with the levels,  ${}^2\text{H}_{11/2}$  and  ${}^4\text{S}_{3/2}$ , respectively.  $\Delta E$  is the energy gap between the two levels,  $k$  is the Boltzmann constant, and  $T$  is the absolute temperature. In general, the energy associated with  ${}^2\text{H}_{11/2}$  level is higher than that associated with  ${}^4\text{S}_{3/2}$  level, i.e., particle density  $n_H$  is lower than  $n_S$ , thus, the transition intensity of  ${}^2\text{H}_{11/2} \rightarrow {}^4\text{I}_{15/2}$  is weaker than

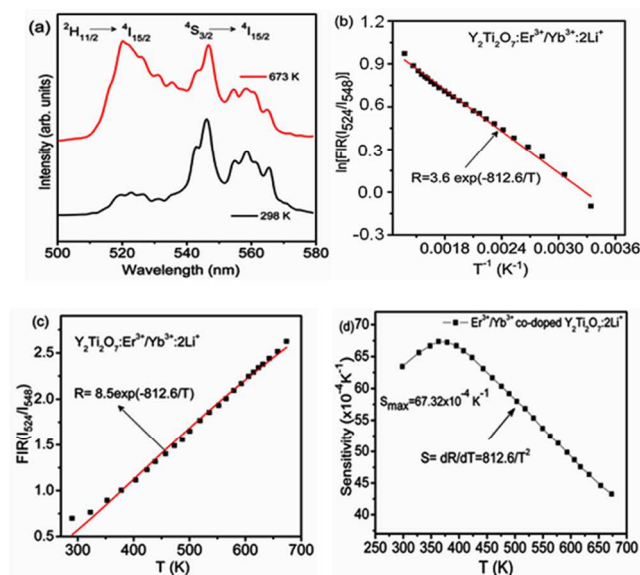


**Fig. 10** Upconversion-based temperature-sensing behaviour of 2 at% Li<sup>+</sup> co-doped Y<sub>2</sub>Ti<sub>2</sub>O<sub>7</sub>:Er<sup>3+</sup>/Yb<sup>3+</sup> phosphor, (a) green up-conversion emission spectra measured at 298 and 673 K, (b) monolog plot of the FIR (using 524 and 548 nm emissions) as a function of the inverse absolute temperature, (c) FIR relative to the temperature, and (d) sensor sensitivity as a function of temperature.

that of  ${}^4\text{S}_{3/2} \rightarrow {}^4\text{I}_{15/2}$  at 298 K, as shown in Fig. 10(a). For high temperature, the energy separation of these two levels requires the  ${}^2\text{H}_{11/2}$  level to be populated by thermal agitation, which in turn provides a higher transition intensity of  ${}^2\text{H}_{11/2} \rightarrow {}^4\text{I}_{15/2}$  than  ${}^4\text{S}_{3/2} \rightarrow {}^4\text{I}_{15/2}$ . The overall intensity of green band decreases as the sample temperature increases. This is probably because of an enhanced lattice vibration followed by non-radiative decay

channel rates. The temperature-dependent up-converted green emission can be attributed to the highly stable spectra in the measured temperature range, i.e., 673 K. Thus, it has great potential in display devices. The relative population density of two thermally populated  ${}^2\text{H}_{11/2} \rightarrow {}^4\text{I}_{15/2}$  and  ${}^4\text{S}_{3/2} \rightarrow {}^4\text{I}_{15/2}$  levels follow the Maxwell Boltzmann distribution, which led to the variation in these two thermally populated levels of fluorescence intensity.

The variation in the FIR of thermally coupled and closely spaced up-conversion bands can be expressed as follows:<sup>23,49,50</sup>

$$R = \frac{I_H}{I_S} = \frac{n_H}{n_S} = \frac{g_H \omega_H \sigma_H}{g_S \omega_S \sigma_S} \exp\left(\frac{-\Delta E}{kT}\right) \quad (\text{iii})$$

where  $I_H$ ,  $I_S$ ,  $\omega_H$ ,  $\omega_S$ ,  $\sigma_H$ , and  $\sigma_S$  are the corresponding intensities, transition frequencies of the associated levels, and the absorption probability rates of  ${}^2\text{H}_{11/2}$  and  ${}^4\text{S}_{3/2}$  levels to the  ${}^4\text{I}_{15/2}$  level, respectively, while  $n_H$ ,  $n_S$ ,  $g_H$ , and  $g_S$  are defined as in equation (ii).

$$R = B \exp\left(\frac{-\Delta E}{kT}\right) \quad (\text{iv})$$

where  $B$  is the pre-exponential factor and  $\Delta E$ ,  $k$ , and  $T$  have the same meaning as defined in equation (ii). From the above equation (iv), clearly FIR is independent of source intensity, which is the prerequisite of any temperature measuring sensing device. The variation in FIR to the relative bands centred at 524 and 548 nm as a function of inverse absolute temperature on a monolog scale is shown in Fig. 10(b). The linear dependency of the curve demonstrates the suitability of the material in temperature-sensing applications.

A fitted slope value obtained by fitting a straight line equation was found to be  $\sim 812 \pm 6.24$  for the curve shown in the figure. The  $B$  value obtained using equation (iv), for the best curve fitting of the experimental data, is 8.5 (as shown in Fig. 10(c)).

The up-converted intensity of green band has been monitored at different power density and it shows that two bands centred at 524 and 548 nm reflect different intensity variation (Shown in Fig. S3 (a)). Moreover, the FIR has been monitored as a function of laser input power density at room temperature and it has been observed that variation in these two bands depend on laser input power density (Shown in Fig. S3 (b)). As  $B$  values varies for different sets of samples so equation (iv) can be modified as:

$$\ln\left(\frac{I_{524}}{I_{548}}\right) = \ln B - \frac{\Delta E}{kT} \quad (\text{v})$$

where all the terms has usual meaning as defined above. Similar behaviour was reported Eu<sup>3+</sup>/Er<sup>3+</sup>/Yb<sup>3+</sup> co-doped Y<sub>2</sub>O<sub>3</sub> system.<sup>51</sup>

Furthermore, the rate of the change of FIR with respect to temperature is a prominent parameter to demonstrate the utility of the present material as a temperature sensor, termed as sensor sensitivity<sup>52</sup>(S), and defined as follows:

$$S = \frac{d(\text{FIR})}{dT} = \text{FIR} \times \left(\frac{-\Delta E}{kT^2}\right) \quad (\text{vi})$$

where  $S$  is the sensor sensitivity and the other terms have usual meanings as defined earlier.

The sensor sensitivity was calculated using equation (vi) as a

function of the temperatures plotted in Fig. 10(d). The sensor sensitivity enhanced with increasing sample temperature, thus clearly indicating that this material can be used as a temperature-sensing probe. The maximum sensitivity at 363 K was found to be  $\sim 67.32 \times 10^{-4} \text{ K}^{-1}$ . Similar studies have been reported by Dong *et al.*<sup>6</sup> for Er-Mo:Yb<sub>2</sub>Ti<sub>2</sub>O<sub>7</sub> phosphors, with sensitivity of  $\sim 0.0074 \text{ K}^{-1}$  in the temperature range  $\sim 295$ – $610 \text{ K}$ . It is worthwhile to compare the sensitivity results of the developed EYYTO:2Li phosphor with similar studies on other materials.<sup>53–58</sup> Y<sub>2</sub>Ti<sub>2</sub>O<sub>7</sub>:Er<sup>3+</sup>/Yb<sup>3+</sup>:2Li phosphor is a better material for optical sensors both in terms of temperature range and sensor sensitivity. Moreover, the emission intensities were very stable in the measured temperature, i.e. 673K, which corroborates its utility at higher temperatures as well. We could not study the performance beyond this temperature range because of instrumental limitations. The results demonstrate that YTO is a good host matrix (melting point  $\sim 1600 \text{ }^\circ\text{C}$ )<sup>59</sup> for up-conversion based phosphors, which can be substantially used in display devices and over wide temperature ranges with high-sensitivity temperature sensors.

#### 4.4 CIE study

The Colour perception of the samples is demonstrated by mathematically defined colour chromaticity diagram (as shown in Fig.11). Clearly, the Commission Internationale de l'Eclairage (CIE) diagram shows that the Li<sup>+</sup>-co-doping samples lie towards the pure green region. The typical CIE plots of EYYTO and EYYTO:2Li were calculated, indicating that the Li<sup>+</sup> co-doped phosphors show better improvement in the purity of green colour emitted from the prepared samples.

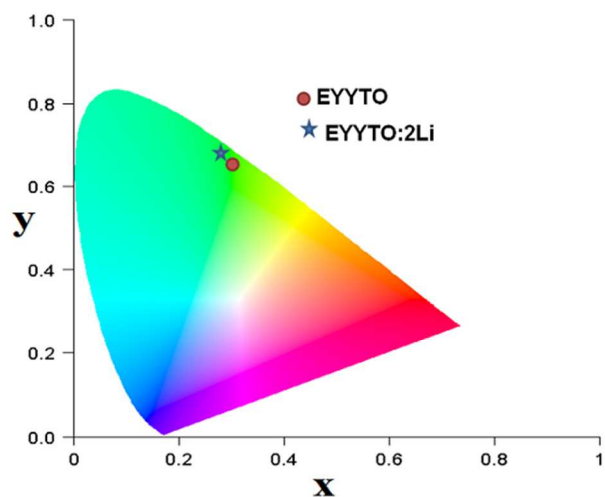


Fig.11 CIE diagram for Li<sup>+</sup> (0 and 2 at%) co-doped Y<sub>2</sub>Ti<sub>2</sub>O<sub>7</sub>:Er<sup>3+</sup>/Yb<sup>3+</sup>.

#### 4.5 Decay analysis

The decay profile of green band ( $\sim 548 \text{ nm}$ )  $^4\text{S}_{3/2} \rightarrow ^4\text{I}_{15/2}$  for EYYTO:2Li under 976 nm excitation was measured. Fig. 12 shows the normalised decay curve of  $\sim 548 \text{ nm}$  band for the green bands. The decay profile may be well fitted to a mono-exponential function as follows:

$$I = I_0 + A_1 \exp\left(\frac{-t}{\tau}\right) \quad (\text{vii})$$

where  $I_0$  and  $I$  are the initial intensity and intensity at time  $t$ , respectively.  $A_1$  is a constant,  $t$  is the time, and  $\tau$  is the decay time of the emitting level. The lifetime of  $^4\text{S}_{3/2}$  state was found to be  $\sim 548 \mu\text{s}$ , which is higher than that of Li<sup>+</sup>-free EYYTO sample.<sup>11</sup> The monoexponential fitting and its residuals are shown in the Fig. inset. The prolonged decay time of EYYTO:2Li can be attributed to the tailored local environment around Er<sup>3+</sup> ions.

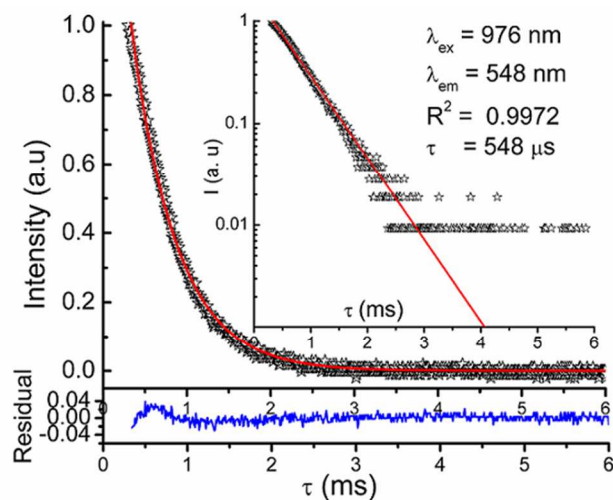


Fig.12 Decay curve of EYYTO:2Li phosphor at 548 nm ( $^4\text{S}_{3/2} \rightarrow ^4\text{I}_{15/2}$ ) band under 976 nm excitation.

## 5. Conclusions

Li co-doped Y<sub>2</sub>Ti<sub>2</sub>O<sub>7</sub>:Er<sup>3+</sup>/Yb<sup>3+</sup> phosphors were synthesized by a solid-state ceramic method. The structures of the phosphors were analysed in detail by Rietveld XRD, XPS, FTIR, FE-SEM, Raman and PL measurements. The XRD study confirmed the pyrochlore phase with a *fcc* structure. The XPS study revealed the characteristic valence states and associated oxygen vacancies on the sample surface. Raman spectroscopy reveals the surface defects associated with the sample and structure corroborates to its pyrochlore type feature and its  $r_A/r_B$  ratio decreases with Li<sup>+</sup> ion concentration. Significantly enhanced green and red emissions were observed after introducing Li<sup>+</sup> ions, which may tailor the environment of surrounding Er<sup>3+</sup> ions. With Li<sup>+</sup> ion inclusion, the decay profile of the green bands (548 nm) corroborates the prolonged decay time value as compared to the Li<sup>+</sup>-free sample. The temperature-dependent FIR study corroborates the applicability of this phosphor material in the development of an optical temperature sensor with high sensitivity over a wide temperature range. The maximum sensitivity was found to be  $\sim 0.0067 \text{ K}^{-1}$  at 363 K. EYYTO:2Li phosphor may be used in the development of an efficient green up-converter and temperature sensor having a wide temperature range and with high efficacy.

## Acknowledgements

One of the authors (B. P. Singh) acknowledges the financial support from the Ministry of Human Resources and Development (MHRD) in the form of teaching assistantship. The authors also

acknowledge Dr. V. K. Rai Dept. of Applied Physics, ISM, Dhanbad, India, for providing the up-conversion and temperature sensor facilities.

#### Authors Affiliations:

<sup>a</sup>Department of Physics, Indian Institute of Technology (BHU), Varanasi, India-221005; <sup>b</sup>Department of Physics, Banaras Hindu University, Varanasi, India-221005; <sup>c</sup>Department of Biological Engineering, Utah State University, Logan, Utah, USA-84322; <sup>d</sup>Chemistry Division Bhabha Atomic Research Centre, Mumbai, India-400085; <sup>e</sup>Department of Physics, Andhra University, Visakhapatnam, India-530003; <sup>f</sup>Department of Physics, Sfax University, Sfax, Tunisia-3018; \*E-mail of Corresponding Author: ak.parchur@usu.edu and karemskpa@hotmail.com

## References

1. S. Siva Kumar, F. C. J. M. van Veggel, M. Raudsepp, *J. Am. Chem. Soc.*, 2006, **128**, 2115.
2. R. Neccache, F. Vetrone, V. Mahalingam, L. A. Cuccia and J. A. Capobianco, *Chem. Mater.*, 2009, **21**, 717.
3. V. M. vander Ende, L. Arts and A. Meijerink, *Phys. Chem. Chem. Phys.*, 2009, **11**, 11081.
4. J. C. Boyer, L. A. Cuccia and J. A. Capobianco, *Nano Lett.*, 2007, **7**, 847.
5. B. K. Gupta, V. Rathee, T. N. Narayanan, P. Thanikaivelan, A. Saha, Govind, S. P. Singh, A. A. Marti and P. M. Ajayan, *Small*, 2011, **7**, 1767.
6. B. Dong, B. Cao, Y. He, Z. Liu, Z. Li and Z. Feng, *Adv. Mater.*, 2012, **24**, 1987.
7. F. Wang, R. R. Deng, J. Wang, Q. X. Wang, Y. Han, H. M. Zhu, X. Y. Chen and X. G. Liu, *Nat. Mater.*, 2011, **10**, 968.
8. G. Y. Chen, T. Y. Ohulchanskyy, A. Kachynski, H. Agren and P. N. Prasad, *ACS Nano*, 2011, **5**, 4981.
9. A. A. Ansari, T. N. Hasan, N. A. Syed, J. P. Labis, A. K. Parchur, G. Shafi, and A. A. Alshatwai, *Nanomedicine*, 2013, **9**, 1328.
10. C. C. Ting, Y. S. Chiu, C. W. Chang and L. C. Chuang, *J. Solid State Chem.*, 2011, **184**, 563.
11. B. P. Singh, A. K. Parchur, R. K. Singh, A. A. Ansari, P. Singh and S. B. Rai, *Phys. Chem. Chem. Phys.*, 2013, **15**, 3480.
12. A. Patra, C. S. Friend, R. Kapoor and P. N. Prasad, *Appl. Phys. Lett.*, 2003, **83**, 284.
13. A. Kar and A. Patra, *Nanoscale*, 2012, **4**, 3608.
14. A. K. Parchur, A. A. Ansari, B. P. Singh, F. N. Syed, T. N. Hasan, S. B. Rai and R. S. Ningthoujam, *Integr. Biol.*, 2014, **6**, 53.
15. G. S. Yi and G. M. Chow, *Adv. Funct. Mater.*, 2006, **16**, 2324.
16. N. Dhananjaya, H. Nagabhushana, B. M. Nagabhushana, B. Rudraswamy, C. Shiva Kumar and R. Chakradhar, *J. Alloys Compd.*, 2011, **509**, 236.
17. Q. Cheng, J. Sui and W. Cai, *Nanoscale*, 2012, **4**, 779.
18. A. K. Parchur and R. S. Ningthoujam, *RSC Adv.*, 2012, **2**, 10854.
19. G. Y. Chen, H. C. Liu, H. J. Liang, G. Somesfalean and Z. G. Zhang, *J. Phys. Chem. C*, 2008, **112**, 12030.
20. H. Q. Wang and T. Nann, *ACS Nano*, 2010, **4**, 1768.
21. Y. Bai, K. Yang, Y. Wang, X. Zhang and Y. Song, *Optics Commun.* 2008, **281**, 2930.
22. D. Li, Y. Wang, X. Zhang, H. Dong, L. Liu, G. Shi and Y. Song, *J. Appl. Phys.*, 2012, **112**, 094701.
23. S. A. Wade, S. F. Collins and G. W. Baxter, *J. Appl. Phys.*, 2003, **94**, 4743.
24. V. K. Rai, A. Pandey and R. Dey, *J. Appl. Phys.*, 2013, **113**, 083104.
25. D. S. Brites, P. P. Lima, N. J. O. Silva, A. Mallán, V. Amaral, F. Palacio and L. d. Carlos, *New J. Chem.*, 2011, **35**, 1177.
26. L. Li, C. Guo, S. Jiang, D. K. Agrawal and T. Li, *RSC Adv.*, 2014, **4**, 6391.
27. R. D. Shanon, *Acta Crystallogr., Sect. A: Cryst. Phys.*, 1976, **32**, 751.
28. J. Rodríguez-Carvajal, *FULLPROF* a Rietveld and pattern matching analysis program, Laboratoire Leon Brillouin (CEA-CRNS), Paris France.
29. P. Mandal, A. Banerji, V. Sathe, S. K. Deb and A. K. Tyagi, *J. Solid State Chem.*, 2007, **180**, 2643.
30. M. A. Subramanian, G. Aravamudan and G. V. S. Rao, *Prog. Solid State Chem.*, 1983, **15**, 55.
31. G. Sala, M. J. Gutmann, D. Prabhakaran, D. Pomaranski, C. Mitchelitis, J. B. Kycia, D. G. Porter, C. Castelnovo and J. P. Goff, *Nat. Mater.*, 2014, **13**, 488.
32. A. K. Parchur, A. I. Prasad, S. B. Rai, R. Tewari, R. K. Sahu, G. S. Okram, R. A. Singh and R. S. Ningthoujam, *AIP Adv.*, 2012, **2**, 032119.
33. S. Huang, L. Gu, C. Miao, Z. Lou, N. Zhu, H. Yuan and A. Shan, *J. Mater. Chem. A*, 2013, **1**, 7874.
34. J. Christopher and C. S. Swamy, *J. Mater. Sci.*, 1991, **26**, 4966.
35. T. Jia, Y. Liu, H. Zhao, H. Du, J. Sun, G. Ge, *J. Solid State Chem.*, 2010, **183**, 584.
36. S. Saha, S. Das, U. K. Ghorai, N. Mazumder, B. K. Gupta and K. K. Chattopadhyay, *Dalton Trans.*, 2013, **42**, 12965.
37. M. L. Sanjuán, C. Guglieri, S. Díaz-Moreno, G. Aquilanti, A. F. Fuentes, L. Olivi and J. Chaboy, *Phys. Rev. B*, 2011, **84**, 104207.
38. S. Brown, H. C. Gupta, J. A. Alonso and M. J. M. Lope, *J. Raman Spectrosc.*, 2003, **34**, 240.
39. S. A. Camacho, P. H. B. Aoki, C. J. L. Constantino, R. F. Aroca and A. M. Pires, *J. Alloys Compd.*, 2012, **541**, 365.
40. F. N. Sayed, V. Grover, K. Bhattacharyya, D. Jain, A. Arya, C. G. S. Pillai and A. K. Tyagi, *Inorg. Chem.*, 2011, **50**, 2354.
41. T. Osaka and I. Shindo, *J. Mater. Sci.*, 1984, **51**, 421.
42. T. Fan, Q. Zhang and Z. Jiang, *Optics Commun.*, 2011, **284**, 1594.
43. L. Sun, C. Qian, C. Liao, X. Wang and C. Yan, *Solid State Commun.*, 2001, **119**, 393.
44. O. A. Lopez, J. McKittrick and L. E. Shea, *J. Lumin.*, 1997, **71**, 1.
45. M. Pollnau, D. R. Gamelin, S. R. Luthi, H. U. Gudel and M. P. Hehlen, *Phys. Rev. B*, 200, **61**, 3337.
46. I. Etchart, M. Berard, M. Laroche, A. Huignard, I. Hernandez, W. P. Gillin, R. J. Curry and A. K. Cheetham, *Chem. Commun.*, 2011, **47**, 6263.
47. C. Strohhofer and A. Polman, *Opt. Mater.*, 2003, **21**, 705.
48. L. H. Fischer, G. S. Harms and O. S. Wolfbeis, *Angew. Chem., Int. Ed.*, 2011, **50**, 4546.
49. V. K. Rai, D. K. Rai and S. B. Rai, *Sens. Actuators, A*, 2006, **128**, 14.
50. X. Wei, L. C. Ren, C. B. Sheng and D. Bin, *Chin. Phys. B*, 2010, **19**, 127804.
51. R. De, A. Pandey, V. K. Rai, *Sens. Actuators, B*, 2014, **190**, 512.
52. W. Xu, X. Gao, L. Zheng, Z. Zhang and W. Cao, *Opt. Express*, 2012, **20**, 18127.
53. C. Li, S. Li, B. Dong, Z. Liu, C. Song and Q. Yu, *Sens. Actuators, B*, 2008, **134**, 313.
54. L. Liu, Y. Wang, X. Zhang, K. Yang, Y. Bai, C. Huang and Y. Song, *Opt. Commun.*, 2011, **248**, 1876.
55. N. Rakov and G. S. Maciel, *Sens. Actuators, B*, 2012, **164**, 96.
56. C. Li, B. Dong, C. Ming and M. Lei, *Sensors*, 2007, **7**, 2652.
57. B. Dong, D. P. Liu, X. J. Wang, T. Yang and S. M. Miao, *Appl. Phys. Lett.*, 2007, **90**, 181117.
58. S. F. León-Luis, U. R. Rodríguez-Mendoza, E. Lalla and V. Lavín, *Sens. Actuators, B*, 2011, **158**, 208.
59. M. B. Johnson, D. D. James, A. Bourque, H. A. Dabkowska, B. D. Gaulin and M. A. White, *Journal of Solid State Chemistry*, 2009, **182**, 725.